PCCP

Air separation via two-step solar thermochemical cycles based on SrFeO3-δ and (Ba,La)0.15Sr0.85FeO3-δ perovskite reduction/oxidation reactions to produce N2: Rate limiting mechanism(s) determination

SCHOLARONE™
Manuscripts

Air separation via two-step solar thermochemical cycles based on SrFeO$_{3-\delta}$ and (Ba,La)$_{0.15}$Sr$_{0.85}$FeO$_{3-\delta}$ perovskite reduction/oxidation reactions to produce N$_2$: Rate limiting mechanism(s) determination

Nhu Pailes Nguyen[1], Tyler Farr[1], H. Evan Bush[2], Andrea Ambrosini[2], Peter G. Loutzenhiser[1*]

[1]George W. Woodruff School of Mechanical Engineering, Georgia Institute of Technology, Atlanta, Georgia USA, 30332-0405

[2]Concentrating Solar Technologies, Sandia National Laboratories, P.O. Box 5800 MS0734, Albuquerque, NM 87185 USA

*Corresponding Author: Peter G. Loutzenhiser, Email: peter.loutzenhiser@me.gatech.edu
Phone: +1.404.894.3012

Abstract

Two-step solar thermochemical cycles based on reversible reactions of SrFeO$_{3-\delta}$ and (Ba,La)$_{0.15}$Sr$_{0.85}$FeO$_{3-\delta}$ perovskites were considered for air separation. The cycle steps encompass (1) the thermal reduction of SrFeO$_{3-\delta}$ or (Ba,La)$_{0.15}$Sr$_{0.85}$FeO$_{3-\delta}$ perovskites driven by concentrated solar irradiation and (2) oxidation in air to remove O$_2$ and produce N$_2$. Rate limiting mechanisms were examined for both reactions using a combination of isothermal and non-isothermal thermogravimetry for temperature-swings between 673 and 1373 K, heating rates of 10, 20, and 50 K/min, and O$_2$ pressure-swings between 20% O$_2$/Ar and 100% Ar at atmospheric pressure. Evolved O$_2$ and associated lag due to transport behavior were measured with gas chromatography and used with measured sample temperatures to predict equilibrium compositions from a compound energy formalism thermodynamic model. Measured and predicted chemical equilibrium changes in deviation from stoichiometry were compared. Rapid chemical kinetics were observed as the samples equilibrated rapidly for all conditions, indicative that heat and mass transfer were the rate limiting mechanisms. The effects of bulk diffusion (or gas diffusion through the bed or pellet) were examined using pelletized and loose powdered samples and determined to have no discernable impact.

Keywords: SrFeO$_{3-\delta}$, kinetics, air separation, concentrating solar

1. Introduction

In previous works, an A- and B-site substitutional study of $SrFeO_{3-\delta}$ [1] and compound energy formalism thermodynamic model of $SrFeO_{3-\delta}$ and $(Ba, La)_xSr_{1-x}FeO_{3-\delta}$ with $0 \leq x \leq 0.2$ [2] were employed to examine solar thermochemical air separation. Two-step cycles were employed based on the following reversible reactions to produce N_2, represented in Kröger–Vink notation as:

$$2Fe_{Fe}^{\times} + O_O^{\times} \rightleftharpoons 2Fe_{Fe}' + V_O^{\bullet\bullet} + \frac{1}{2}O_2(g) \tag{1}$$
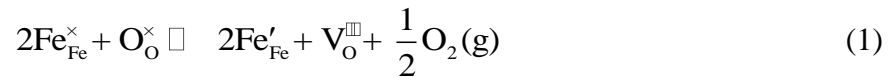
where $V_O^{\bullet\bullet}$ represents a O^{2-} vacancy; $Fe_{Fe}^{\times}$ and $O_O^{\times}$ are the neutral ions; Fe_{Fe}' is the negatively charged ion; and the non-labile Sr^{2+} and Ba^{2+} or La^{3+} are omitted. The cycle is depicted schematically in Figure 1.
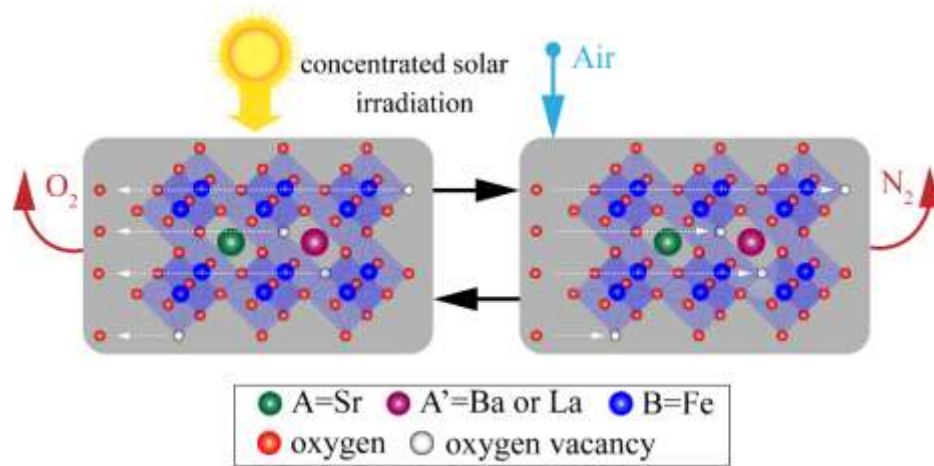

Figure 1. Schematic of the two-step solar thermochemical air separation cycle based on reversible reduction/oxidation reactions of $SrFeO_{3-\delta}$ or $(Ba,La)_{0.15}Sr_{0.85}FeO_{3-\delta}$.

The cycle steps encompass the following:

1. The thermal reduction of $Fe^{4+} \rightarrow Fe^{3+}$ on the B-site using process heat from concentrated solar irradiation to achieve elevated temperatures. $V_O^{\bullet\bullet}$ are formed as $O^{2-} \rightarrow \frac{1}{2}O_2(g)$ to maintain electroneutrality.

2. The oxidation of $Fe^{3+} \rightarrow Fe^{4+}$ in air at lower temperatures off-sun where $V_O^{\bullet\bullet}$ sites are filled by O_2 from the air resulting in high-purity N_2. The oxidized $SrFeO_{3-\delta}$ or $(Ba, La)_xSr_{1-x}FeO_{3-\delta}$ samples are recycled back to the first step to complete the cycle.

SrFeO$_{3-\delta}$ and (Ba,La)$_{0.15}$Sr$_{0.85}$FeO$_{3-\delta}$ with mixed ionic-electronic conducting (MIEC) properties exhibit rapid reaction kinetics due to facile oxygen transport through the sublattice in the absence of crystal structure changes [3]. Understanding the rate limiting mechanism(s) is an essential activity for guiding the development of solar thermochemical and oxidation reactors to efficiently realize both cycle steps. Foundational work with SrFeO$_{3-\delta}$ [4], substituted SrFeO$_{3-\delta}$ [3, 5-12], La$_x$Sr$_{1-x}$Co$_y$Fe$_{1-y}$O$_{3-\delta}$ [13, 14], and Ba$_x$Sr$_{1-x}$Co$_y$Fe$_{1-y}$O$_{3-\delta}$ [15] was carried out to examine and characterize the materials for air separation and other solar thermochemical applications. The materials are well-suited for these applications due to cyclability between reduction/oxidation (redox) reactions below sintering temperatures [6] with low reaction enthalpies and high redox capacities. Oxygen capacities were determined to be highly dependent on the oxygen vacancy concentration in substituted SrFeO$_{3-\delta}$ [12]. High oxygen vacancy formation and oxygen diffusion rates [3, 5, 16-18] also contribute to rapid oxygen exchange [19, 20]. Isothermal relaxation was previously used to quantify the chemical kinetics of SrFeO$_{3-\delta}$ between 523 and 723 K, suggesting that oxidation chemical kinetics become rate limiting at < 550 K [21]. A significant half-life for the reduction of SrFeO$_{3-\delta}$ was observed > 600 K under 1% O$_2$/inert gas. A point defect model combined with a cluster model was coupled with thermogravimetry to investigate redox kinetics of SrFeO$_{3-\delta}$ and SrMn$_{0.1}$Fe$_{0.9}$O$_{3-\delta}$ in packed beds [10]. Both materials were shown to oxidize quickly above 798 K, and the packed bed O$_2$ uptake was faster than the O$_2$ supply from the sweep gas. Significant differences between reduction and oxidation rates were observed for La$_{0.4}$Sr$_{0.6}$FeO$_{3-\delta}$ at extremely low O$_2$ partial pressure < 10$^{-2.7}$ bar for temperatures between 973 and 1173 K [22]. The oxygen exchange rate in La$_{0.4}$Sr$_{0.6}$FeO$_{3-\delta}$ was observed to be surface-controlled and independent of sample depth, indicating that bulk diffusion was likely not the rate limiting mechanism in substituted SrFeO$_{3-\delta}$ redox kinetics. Experimental work with Y$_{0.5}$Ba$_{0.5}$CoO$_{3-\delta}$ indicated faster reaction rates below 800 K and higher redox capacities than SrFeO$_{3-\delta}$, further confirmed by previous work [23].

Chemical kinetics work that was focused on binary metal oxides showed fast oxidation rates (within 20 s) between 673 and 973 K of Fe$_3$O$_4$ to Fe$_2$O$_3$ during O$_2$ pressure-swings from 100% Ar to 80% O$_2$/Ar [24]. Full conversion of CoO to Co$_3$O$_4$ in O$_2$ occurred in < 30 s at 1133 K during isothermal thermogravimetry with O$_2$ pressure-swings between 100% Ar and 20% O$_2$/Ar. Non-isothermal experiments detected an onset of reaction of 430 K [25].

Other studies relevant to solar thermochemistry applications investigated chemical kinetics of a wide range of oxides (*e.g.*, CeO_2 [26], cobalt ferrite $/ZrO_2$ composite [27], $Sr_{0.4}La_{0.6}Mn_{0.6}Al_{0.4}O_3$ and $CaTiO_3$ [28]) for H_2O and CO_2 splitting. CeO_2 doped with Ta was observed to increase reducibility at 1673 K with slower kinetics due to formation of a secondary phase [26]. The redox reactions of a cobalt ferrite $/ZrO_2$ composite for H_2O splitting required > 900 s for oxidation between 1173 and 1673 K in 30% $H_2O/$ He to produce H_2 and > 6000 s during the thermal reduction at 1723 K in He [27], with ionic diffusion identified as the rate limiting mechanism.

The rate limiting mechanism(s) of $SrFeO_{3-\delta}$ and $(Ba,La)_{0.15}Sr_{0.85}FeO_{3-\delta}$ were examined in this work using a combination of isothermal and non-isothermal thermogravimetry. Temperature swings at varying heating rates were used to assess heat transfer limitations between 673 and 1373 K, which are relevant operating temperatures for solar thermochemical air separation. O_2 pressure-swings were conducted to assess potential mass transfer limitations. The impact of bulk diffusion on reaction rates was investigated for powdered and pelletized $Ba_{0.15}Sr_{0.85}FeO_{3-\delta}$ samples. The compound energy formalism (CEF) [2, 29] was used to predict chemical equilibrium deviations from stoichiometry for $SrFeO_{3-\delta}$ and $(Ba,La)_x Sr_{1-x}FeO_{3-\delta}$ as a function of temperature, O_2 partial pressure, and Ba/La site fraction [2] and compared to measured deviations from stoichiometry from the thermogravimetry.

2. Experimental section

$SrFeO_{3-\delta}$ and $(Ba,La)_{0.15}Sr_{0.85}FeO_{3-\delta}$ samples were synthesized to examine rate limiting mechanisms for different conditions. $(Ba, La)_xSr_{1-x}FeO_{3-\delta}$ were identified by employing the standard first-letter convention for perovskites, followed by numbers indicating the *x*: $Ba_{0.15}Sr_{0.8}FeO_{3-\delta} \equiv$ BSF1515 and $La_{0.15}Sr_{0.8}FeO_{3-\delta} \equiv$ LSF1515 for $x = 0.15$.

2.1. Synthesis methodology

Samples were synthesized using a modified Pechini method [30] from nitrate salt precursors (ALFA AESAR, $\geq$98% purity). Citric acid was used as a chelating agent and fully dissolved with the precursors in ultrapure H_2O. The solutions were continuously heated and stirred on a hot plate to drive evaporation and form thick gels. Samples were dehydrated in a drying oven for ~24 h at 383 K, then ground and heated on a hot plate to above 573 K for auto-combustion, resulting in the formation of ash. The ash was ground and calcined for 5 h at 1073 K in a high

temperature box furnace (SENTOTECH $4\times4\times5$ in^3 1600 °C) to remove any remaining organic or nitrate residue. The samples were reground and heated to between 1473 and 1573K for 36 h to form perovskites.

Pellets were produced by dissolving 2 wt.% polyvinyl butyral (Butvar B-98, Acros Organics) in acetone and grinding it with 160.8 mg of sintered powder sample using a mortar and pestle until a homogenous dried mixture was formed. The mixture was pressed using a 13 mm die under 35 MPa to form a pellet, then sintered for 24 h at 1573 K to form a dense pellet ~1 mm thick with 76% porosity. The PVB was burned off in the sintering process.

2.2. Characterization

X-ray diffractometry (XRD, PANalytical X'Pert PRO Alpha-1 diffractometer with Cu Kα radiation) and whole pattern matching (HighScore, PDF-4+ 2020) were used to verify crystalline structures. Particle size distributions were determined using optical microscopy (Keyence VHX-600) with an in-house image processing software.

2.3. Thermogravimetry

The rate limiting mechanisms were investigated with a combination of isothermal and non-isothermal thermogravimetry (TGA, Netzsch STA 449 F3 Jupiter, $\pm$ 1μg). Powdered and pelletized samples were placed on an alumina crucible covered with platinum foil (Sigma Aldrich 0.025mm 99% Pt Foil) to prevent unwanted side reactions with the crucible. The crucible was in direct contact with a thermocouple (S-type, ±1.5 K) to measure the sample temperature over time. Powdered samples were spread evenly to < 1 mm in thickness to mitigate bulk diffusion. O_2 concentrations were measured using mass spectrometry (MS; Omnistar ThermoStar GSD320 Gas Analysis System) coupled with gas chromatography (GC, Agilent 490 Micro GC, 10m Molsieve).

Two TGA schedules with temperature (dashed) and O_2 concentration (solid) shown in Figure 2 were used to examine the reaction rates for (a) lower heating rates (LHR) and (b) higher heating rates (HHR). Total gas flowrates of 200 mL$_N$/min were used for all experiments, where L$_N$ refers to liters at standard conditions: 273 K and 1 bar.
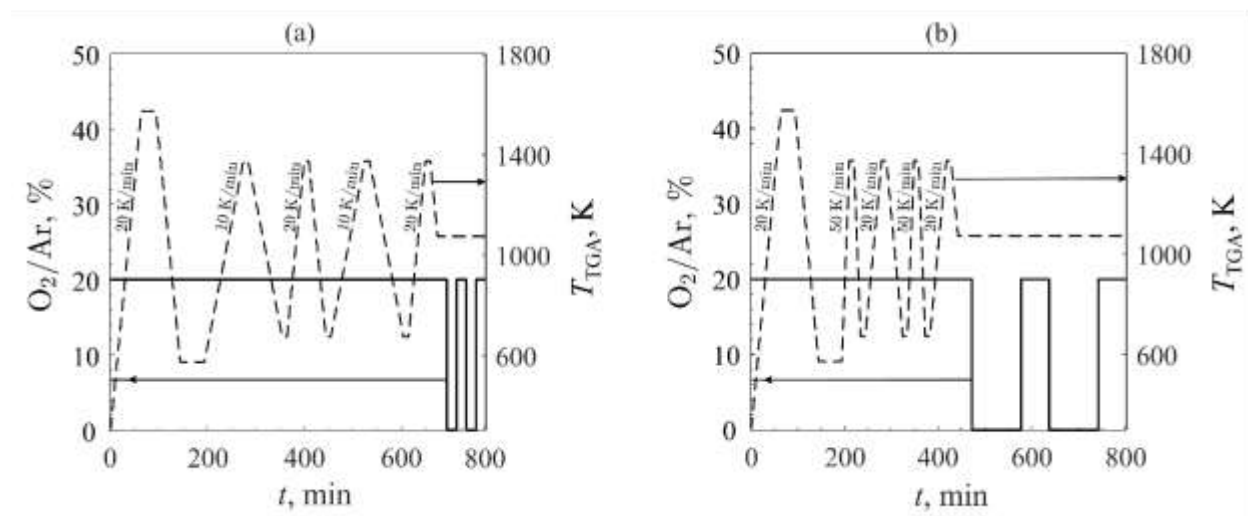
Figure 2. Schedules for kinetics experiments with O_2 concentration in Ar (solid) and temperature (dashed) versus time with (a) lower heating rates of 20 and 10 K/min and (b) higher heating rates of 20 and 50 K/min.

The LHR schedule consisted of 10 K/min and 20 K/min ramps and shorter O_2 pressure-swings of 10 min between 20% O_2/Ar and 100% Ar (Figure 2a). An initial break-in step was performed with the sample heated to a temperature of T_{TGA} = 1573 K at 20 K/min in 20% O_2/Ar (Netzsch mass flow controllers, ±2% accuracy, ±1mL$_N$/min precision), held isothermally for 30 min, cooled to T_{TGA} = 573 K at 20 K/min, and held isothermally at 20% O_2/Ar for 30 min. The break-in step was used to off-gas unwanted adsorbed species in the sample and to standardize the initial deviation from stoichiometry (δ_0). The reference δ_0 was selected at the end of the break-in step at T_{TGA} = 573 K and 20% O_2/Ar when the samples equilibrated. The samples were then cycled between T_{TGA} = 673 and 1373 K four times with alternating heating rates of 10 and 20 K/min. Samples were held isothermally for 10 min between temperature swings. Two O_2 pressure-swing cycles between 20% O_2/Ar and 100% Ar at T_{TGA} = 1073 K followed with 10 min durations between gas changes.

The HHR schedule (Figure 2b) used heating rates of 20 K/min and 50 K/min with longer O_2 pressure-swings. A break-in identical to the LHR schedule was performed. Four temperature swings between 673 and 1373 K and four accompanying isothermal steps were performed with alternating heating/cooling rates of 50 and 20 K/min under 20% O_2/Ar. Samples were held for 10 min at 1373 K after each heating step and 10 min at 673 K after each cooling step during the

temperature swings. Two O_2 pressure-swings at $T_{TGA} = 1073$ K followed with switching between 20% O_2/Ar for 45 min and 100% Ar for 105 minutes.

3. Results and Discussion

Sample characterization and TGA were performed, and chemical equilibrium compositions were determined from a comprehensive thermodynamic model based on the CEF [2]. Changes in deviation from stoichiometry measured by TGA were compared to changes in deviation from stoichiometry at equilibrium to examine reduction and oxidation rate limiting mechanism(s) at heating rates ≤ 50 K/min.

3.1. Characterization

X-ray diffractometry: Diffraction patterns for all samples were matched to the perovskite phase [1]. $SrFeO_{3-\delta}$ samples crystallized in a tetragonal phase while BSF1585 and LSF1585 samples adopted a cubic space group. Pre- and post-TGA XRD taken at room temperature showed no evidence of crystal structure changes or the presence of secondary phases, as seen in Figure 3 for BSF1585 samples, consistent with the observed continuous mass change during the TGA.
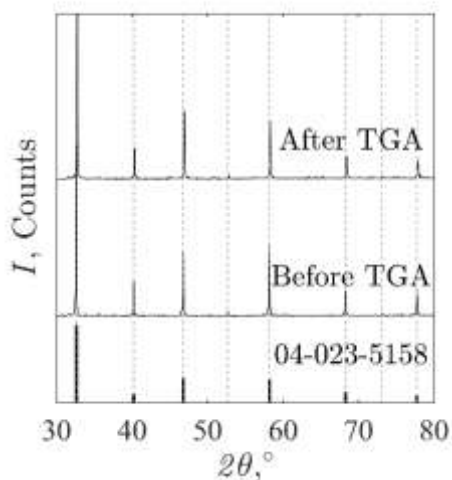

Figure 3. XRD intensity as a function of 2θ for $Ba_{0.15}Sr_{0.15}FeO_{3-\delta}$ before (middle line) and after (upper line) thermogravimetry compared to cubic $SrFeO_{3-\delta}$ (PDF4+ reference number 04-023-5158, bottom pattern). The dashed lines act as a visual guide to the position of 04-023-5158 peaks.

Particle size characterization: Images from optical microscopy (Keyence VHX-600) are shown in Figure 4 for (a) $SrFeO_{3-\delta}$, (b) BSF1585, and (c) LSF1585 particles. The particle shapes were

generally jagged and non-spherical, and all samples showed a visibly wide range of particle sizes.
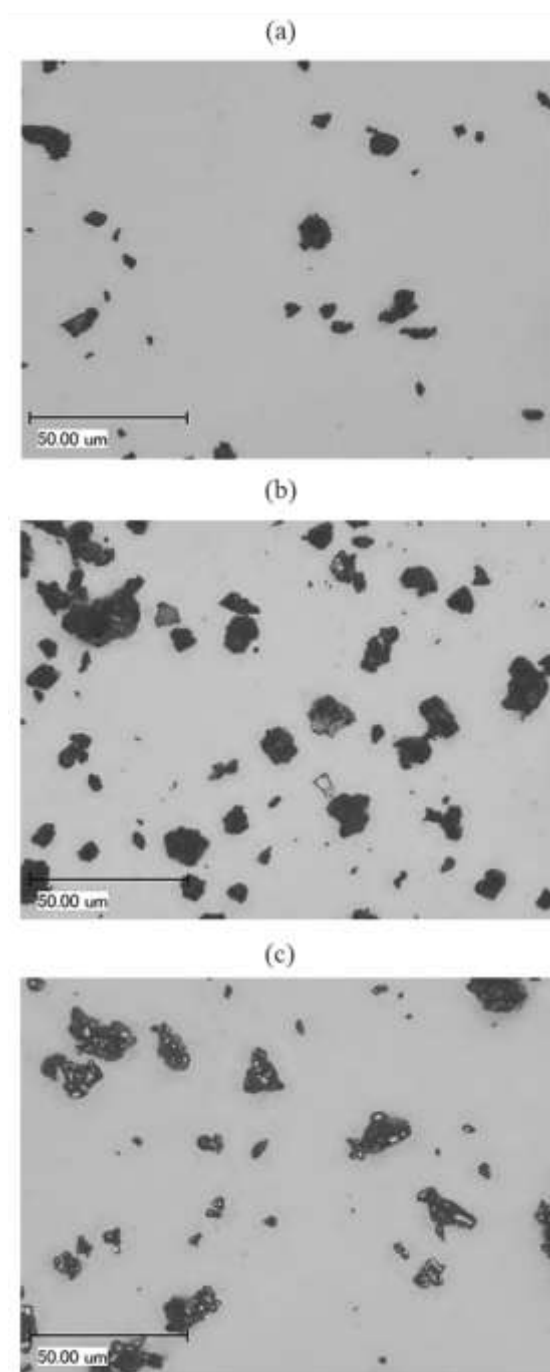

Figure 4. Optical microscopy images of (a) $SrFeO_{3-\delta}$, (b) $Ba_{0.15}Sr_{0.85}FeO_{3-\delta}$ and (c) $La_{0.15}Sr_{0.85}FeO_{3-\delta}$ particles at 1000x magnification using an optical microscope (Keyence VHX-600)

Particle size distributions were determined by coupling optical microscopy with an in-house image processing software. The effective diameter [31, 32] was calculated as:

$$d_{eff} = \frac{4A}{P} \tag{2}$$

where A is the projected area; and P is the perimeter of the particle from the 2D image. d_{eff} distributions are given in Figure 5 for (a) $SrFeO_{3-\delta}$, (b) BSF1585, and (c) LSF1585 particles. The solid line represents a lognormal distribution that best captured the left skewed distribution, resulting from a large number of particle fines. The means and standard deviations of d_{eff} are listed Table 1, showing comparable average particle sizes and deviations between all three samples.
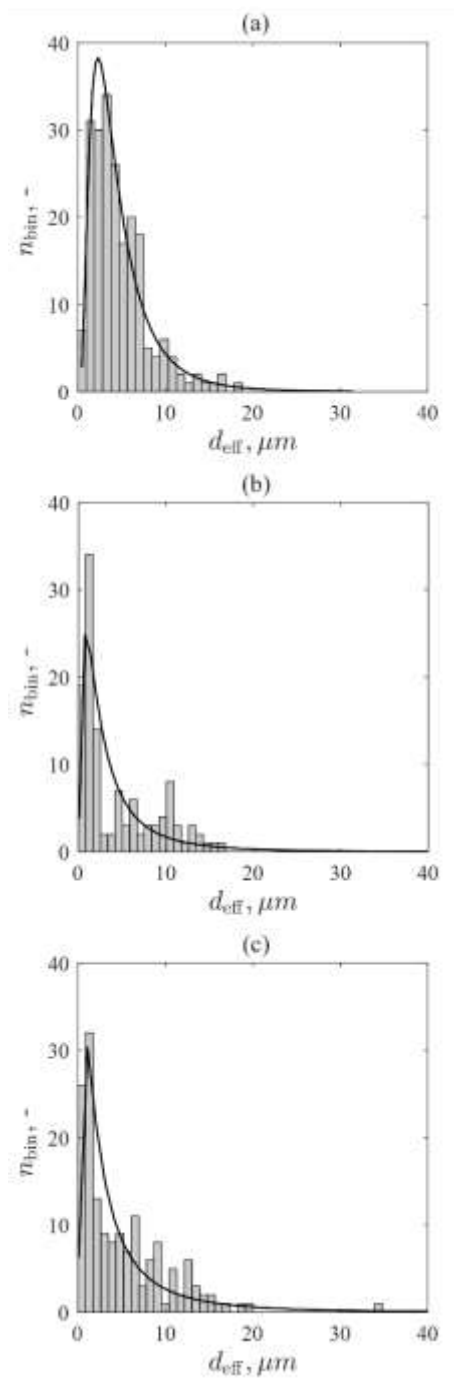
Figure 5. Effective particle size distributions for (a) $SrFeO_{3-\delta}$, (b) $Ba_{0.15}Sr_{0.85}FeO_{3-\delta}$, (c) $La_{0.15}Sr_{0.85}FeO_{3-\delta}$ samples with lognormal distributions (solid lines).

Table 1. Mean effective diameter and standard deviation for $SrFeO_{3-\delta}$, $Ba_{0.15}Sr_{0.85}FeO_{3-\delta}$, and $La_{0.15}Sr_{0.85}FeO_{3-\delta}$ particles

Sample	$\bar{d}_{eff}$, μm	σ, μm
$SrFeO_{3-\delta}$	4.75	3.30
$Ba_{0.15}Sr_{0.85}FeO_{3-\delta}$	4.44	4.32
$La_{0.15}Sr_{0.85}FeO_{3-\delta}$	5.11	5.17

3.2. Thermogravimetry and gas chromatography

TGA was performed on BSF1585, LSF1585, and $SrFeO_{3-\delta}$ powdered samples and a pelletized BSF1585 sample. The changes in deviation from stoichiometry were determined from the TGA as:

$$\Delta\delta_{TGA} = -2\frac{M_O(\delta_0)}{M_{O_2}}\left[\frac{\Delta m}{m_0}\right] \tag{3}$$

where M_O is the molar mass of the sample; M_{O_2} is the molar mass of O_2; Δm is the mass change; δ_0 is the initial sample deviation from stoichiometry after break-in; and m_0 is the initial sample mass. Chemical kinetics were assessed by comparing $\Delta\delta_{TGA}$ and the change in equilibrium deviation from stoichiometry ($\Delta\delta_{equil}$) from the CEF model as a function of O_2 partial pressure, temperature, and the A-site fractions: $\delta_{equil} = f(T_{TGA}, p_{O_2}, x_{Ba}, x_{La})$, where x_{Ba} and x_{La} are the A-site fractions of Ba and La in a sample, respectively. Both $\Delta\delta_{TGA}$ and $\Delta\delta_{equil}$ were determined with the same reference condition of $T_{TGA} = 573$ K and 20% O_2/Ar at 1 bar at the end of the break-in step.

Lower heating rate TGA: The LHR TGA for the BSF1585 powder sample is shown in Figure 6 for (a) O_2/Ar (triangles) measured with GC, T_{TGA} (dashed), and $\Delta\delta_{TGA}$ (solid) and $\Delta\delta_{equil}$ (circles) versus time and (b) a parity plot for temperature (circles) and O_2 pressure swings (solid triangles) where $\Delta\delta_{equil} = \Delta\delta_{TGA}$ is denoted by a solid line. The gas changeovers from 20% O_2/Ar to 100% Ar during the O_2 pressure-swing lagged as O_2 was gradually purged from the system. This gradual purge of O_2 was captured by the GC and impacted the Δm as measured by the TGA. A strong correlation between the predicted $\Delta\delta_{equil}$ and the measured $\Delta\delta_{TGA}$ for the BSF1585 sample was observed during both the temperature- and O_2 pressure-swings. The strong correlation indicated rapid chemical kinetics for temperatures between 673 and 1373 K. A slight vertical

systematic shift was observed between $\Delta\delta_{TGA}$ and $\Delta\delta_{equil}$ due to uncertainties in the CEF and was unaffected by the rapid chemical kinetics. $\Delta\delta_{TGA}$ and $\Delta\delta_{equil}$ were also slightly less correlated during the O_2 pressure-swings, presumably also due to model and experimental uncertainties related to the CEF model and GC limitations due to low temporal resolution. The highest and lowest $\Delta\delta$ were repeatable across all temperature- and O_2 pressure-swings with lower parity seen during the onset of O_2 pressure-swings, resulting in only a few outliers (Figure 6b).
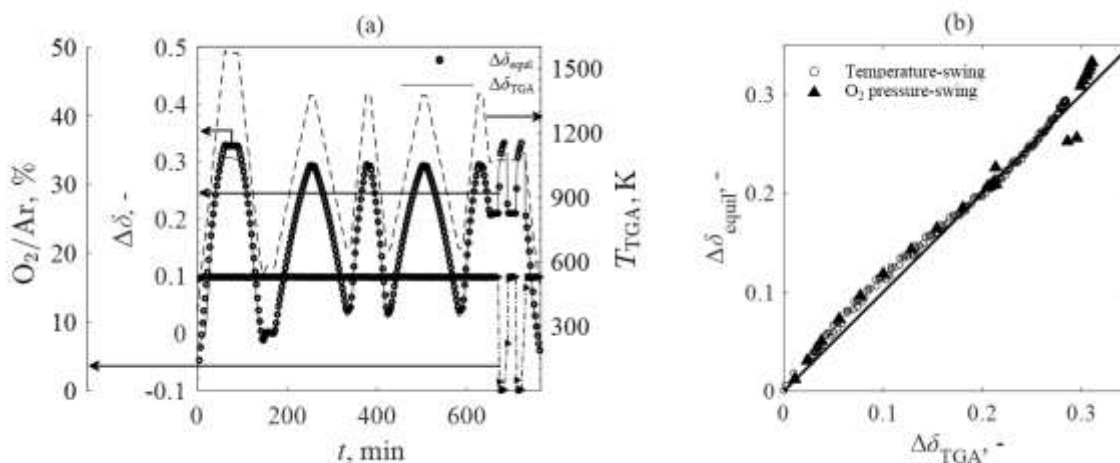

Figure 6. Thermogravimetric analysis of $Ba_{0.15}Sr_{0.85}FeO_{3-\delta}$ powdered sample with heating rates at 20 and 10 K/min for (a) O_2 concentration (triangles) measured with gas chromatography, temperature (dashed line), and changes in deviation from stoichiometry calculated from thermogravimetry (solid line) and calculated at chemical equilibrium (circles) and (b) parity plot comparing the changes in deviation from stoichiometry at chemical equilibrium (solid line) and temperature-(circles) and O_2 pressure-swings (solid triangles).

The LHR experimental results for pelletized BSF1585 are shown in Figure 7 for (a) O_2/Ar(triangles) measured with GC, T_{TGA} (dashed), and $\Delta\delta_{TGA}$ (solid) and $\Delta\delta_{equil}$ (circles) versus time and (b) a parity plot for temperature- (circles) and O_2 pressure-swings (solid triangles) where $\Delta\delta_{equil} = \Delta\delta_{TGA}$ is denoted by a solid line. Rapid reaction rates comparable to the powdered sample were observed during both temperature- and O_2 pressure-swings, indicating that bulk diffusion did not significantly impede the reactions. The pellet thickness mitigates the relative impact of both ionic and bulk diffusion. However, many complex features are involved in the oxygen transport within thick pellets or particle beds. An expected oxygen exchange time of ~ 1 s in a 2.8 mm thick $SrFe_{0.98}Mo_{0.02}O_{3-\delta}$ pellet was previously observed [33], a result of a combination of oxygen transport in the particle inhibited by grain boundaries and O_2 migration through the voids of the dense but porous pellet. The results were consistent with a previous

study of the thermodynamics of $SrFeO_{3-\delta}$, suggesting that O_2 release rate was not dependent on bulk diffusion but on system O_2 removal rate [34]. Minor systematic differences between $\Delta\delta_{TGA}$ and $\Delta\delta_{equil}$ were observed during the temperature-swings for $\Delta\delta$, likely due to the same modeling uncertainties noted for the powdered sample.
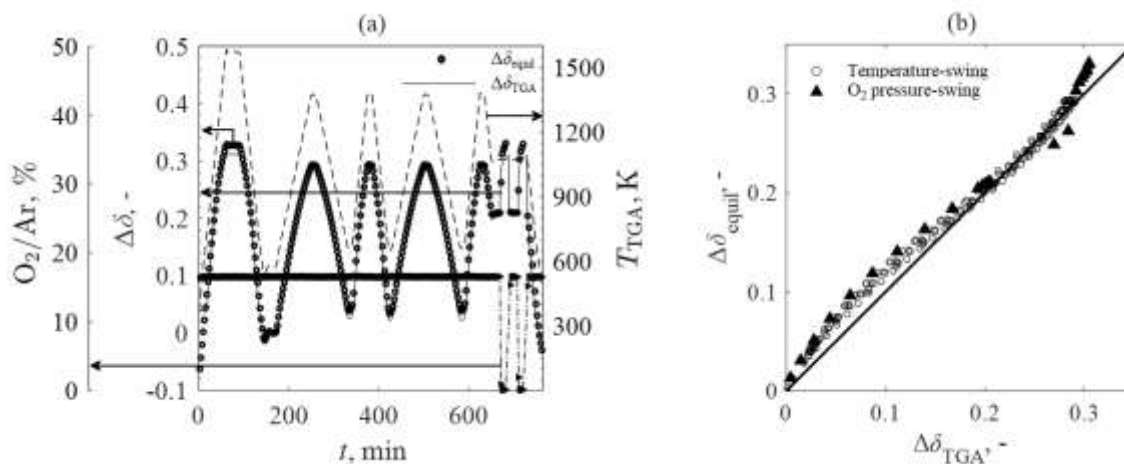

Figure 7. Thermogravimetric analysis of $Ba_{0.15}Sr_{0.85}FeO_{3-\delta}$ pelletized sample with heating rates at 20 and 10 K/min for (a) O_2 concentration (triangles) measured with gas chromatography, temperature (dashed line), and changes in deviation from stoichiometry calculated from thermogravimetry (solid line) and calculated at chemical equilibrium (circles) and (b) parity plot comparing the changes in deviation from stoichiometry at chemical equilibrium (solid line) and temperature- (circles) and O_2 pressure-swings (solid triangles).

Higher heating rate TGA: HHR TGA with heating/cooling rates of 20 K/min and 50 K/min were employed to further examine rate limiting mechanisms. TGA for the LSF1585 powder sample is shown in Figure 8 for (a) O_2/Ar (triangles) measured with GC, T_{TGA} (dashed), and $\Delta\delta_{TGA}$ (solid) and $\Delta\delta_{equil}$ (circles) versus time, (b) a zoomed in view to highlight the changeover from 20% O_2/Ar to 100% Ar, and (c) a parity plot for temperature- (circles) and O_2 pressure-swings (solid triangles) where $\Delta\delta_{equil} = \Delta\delta_{TGA}$ is denoted by a solid line. Rapid chemical kinetics were observed for LSF1585 for both the temperature- and O_2 pressure-swings, and $\Delta\delta_{TGA}$ were strongly correlated with $\Delta\delta_{equil}$ for higher heating rates of 50 K/min. Small systematic errors similar to the LHR experiments were observed for the LSF1585 at higher temperatures during both the temperature- and O_2 pressure-swings. $\Delta\delta_{equil}$ for LSF1585 closely tracked $\Delta\delta_{TGA}$ (Figure 8a) during the temperature-swings, while $\Delta\delta_{TGA}$ equilibrated faster than $\Delta\delta_{equil}$ for O_2 pressure-swings (Figure 8b), consistent with LHR TGA where the low temporal resolution of the GC along with dispersion and lower O_2/Ar concentrations resulted in measurement uncertainties. The

13

results indicated rapid chemical kinetics and heat and mass transfer were the only rate limitations.
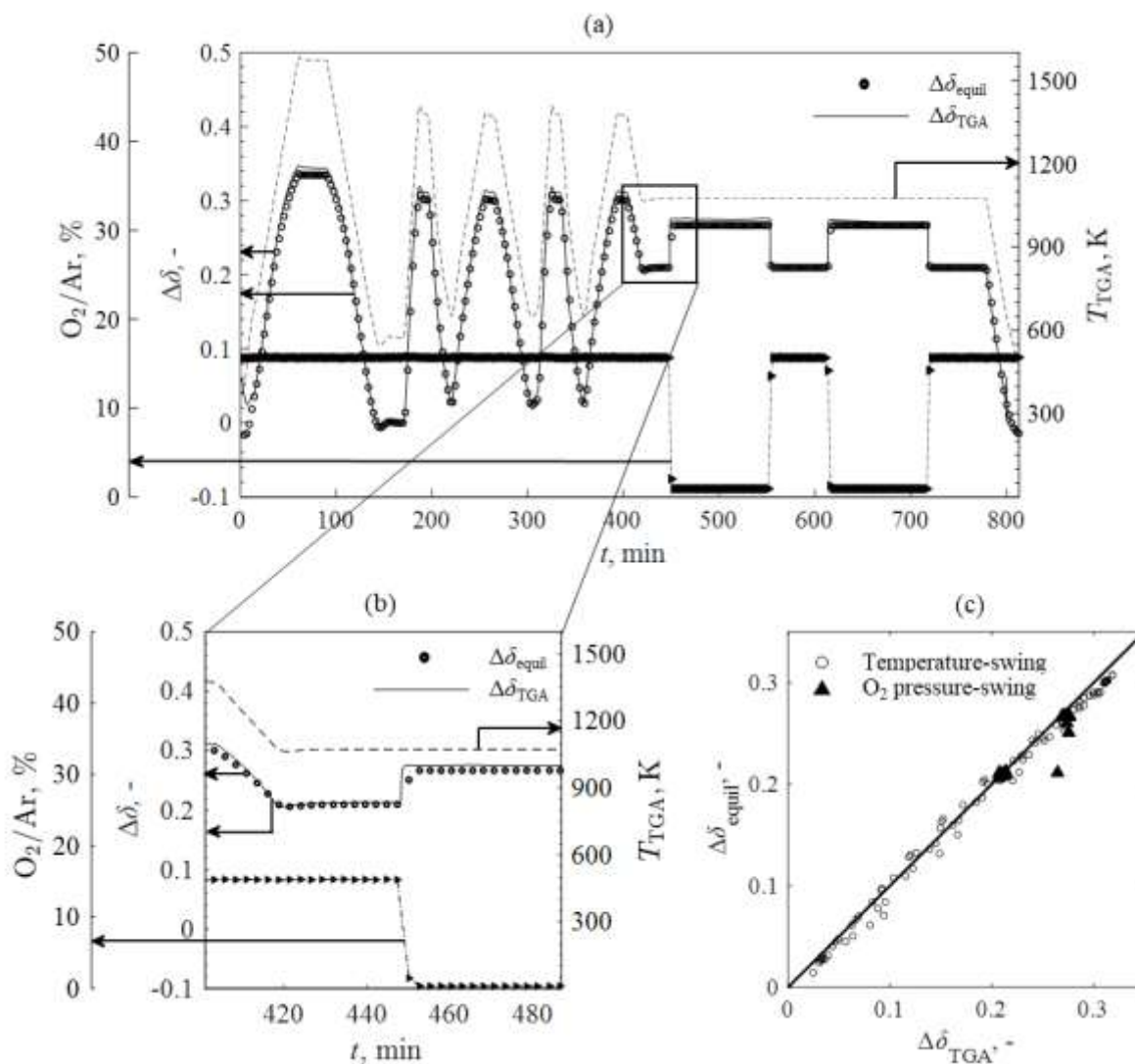

Figure 8. Thermogravimetry analysis with heating rates at 50 and 20 K/min of $La_{0.15}Sr_{0.85}FeO_{3-\delta}$ powdered sample for (a) O_2 concentration (triangles) measured with gas chromatography, temperature (dashed line), and changes in deviation from stoichiometry calculated from thermogravimetry (solid line) and calculated at chemical equilibrium (circles), (b) view of (a) for the initial gas switch during the pressure swing stage and (c) parity plot comparing the changes in deviation from stoichiometry at chemical equilibrium (solid line) and temperature- (circles) and O_2 pressure-swings (solid triangles).

Correlation study: The statistical correlations between $\Delta\delta_{TGA}$ and $\Delta\delta_{equil}$ were examined for all samples for both LHR and HHR TGA using the Pearson correlation coefficient as a metric, given as:

$$r = \frac{n\sum \Delta\delta_{\text{TGA,i}}\Delta\delta_{\text{equil,i}} - \sum \Delta\delta_{\text{TGA,i}} \sum \Delta\delta_{\text{equil,i}}}{\sqrt{n\sum \Delta\delta_{\text{TGA,i}}^2 - \left(\sum \Delta\delta_{\text{TGA,i}}\right)^2}\sqrt{n\sum \Delta\delta_{\text{equil,i}}^2 - \left(\sum \Delta\delta_{\text{equil,i}}\right)^2}} \tag{4}$$

where n is the number of measurands with $-1 \leq r \leq 1$. When r is near unity, strong correlations between $\Delta\delta_{\text{TGA}}$ and $\Delta\delta_{\text{equil}}$ are indicative of reactions in chemical equilibrium that result from rapid chemical kinetics and heat or mass transfer limitations. The r calculated for the temperature- and O_2 pressure-swings are shown in Table 2 for the LHR for all samples. $r \sim 1$ were determined for all samples, indicating rapid chemical kinetics for both unsubstituted and Ba- or La-substituted $SrFeO_{3-\delta}$. This result implies that the substitutions principally affected redox capacities [1] not chemical kinetic and corroborate previous work where variations in the Sr-site content did not produce much difference in ionic oxygen diffusion rate in the material [17]. Similar systematic differences between $\Delta\delta_{\text{TGA}}$ and $\Delta\delta_{\text{equil}}$ were observed for both the $SrFeO_{3-\delta}$ and LSF1585 during the LHR experiments due to the CEF model uncertainties at low O_2/Ar.

Table 2. Pearson correlation coefficients calculated from measured and equilibrium changes in deviation from stoichiometry for $SrFeO_{3-\delta}$ and $(Ba,La)_{0.15}Sr_{0.85}O_{3-\delta}$ samples using lower heating rate thermogravimetry.

Sample	Temperature-swing r, -	O_2 pressure-swing r, -
$SrFeO_{3-\delta}$ (powder)	0.998	0.958
$Ba_{0.15}Sr_{0.85}FeO_{3-\delta}$ (powder)	0.998	0.965
$La_{0.15}Sr_{0.85}FeO_{3-\delta}$ (powder)	0.999	0.964

The r calculated for the temperature- and O_2 pressure-swings are reported in Table 3 for the HHR TGA. The r were determined from all samples equilibrated at 50 K/min, similar to the LHR TGA. Longer O_2 pressure-swing dwells of 105 min compared to 20 min for the LHR TGA facilitated gas stabilization and resulted in higher r for O_2 pressure-swings with mitigated uncertainties associated with gas switching. $\Delta\delta_{\text{TGA}}$ equilibrated faster than $\Delta\delta_{\text{equil}}$ during both HHR and LHR TGA. The d_{eff} appeared to have little to no influence on the results, as the r for the $SrFeO_{3-\delta}$ was similar to $(Ba,La)_{0.15}Sr_{0.85}FeO_{3-\delta}$ for both the LHR and HHR TGA.

Table 3. Pearson correlation coefficients calculated for measured and equilibrium changes in deviation from stoichiometry for $SrFeO_{3-\delta}$ and $(Ba,La)_{0.15}Sr_{0.85}O_{3-\delta}$ samples using higher heating rate thermogravimetry.

Sample	Temperature-swing r, -	O_2 pressure-swing r, -
$SrFeO_{3-\delta}$ (powder)	0.997	0.988
$Ba_{0.15}Sr_{0.85}FeO_{3-\delta}$ (powder)	0.996	0.995
$La_{0.15}Sr_{0.85}FeO_{3-\delta}$ (powder)	0.997	0.985

The findings show that using TGA to measure chemical kinetics between 673 and 1373 K in and 20% O_2/Ar and 100% Ar is problematic for μm-sized particles when using isothermal or non-isothermal thermogravimetry coupled to gas switches. The rapid chemical kinetics from MIEC behavior (*i.e.*, facile oxygen transport through the sublattice in the absence of crystal structure changes) results in materials that rapidly equilibrate for μm-sized particles with short ionic oxygen diffusion pathlengths. TGA studies must be coupled to low O_2 concentration temporal measurements to account for purging during gas switchovers which, when not considered, potentially are misinterpreted as intrinsic chemical kinetics. Introducing chemical kinetics erroneously determined under these conditions presents design challenges. Coupling heat and mass transfer models to inaccurate chemical kinetics leads to overestimation of material residence times, resulting in non-optimized redox reactor performance. Determination of intrinsic chemical kinetics for $SrFeO_{3-\delta}$ -based materials requires rapid heating rates, O_2 changeovers and purges, and precise gas concentration measurements to examine reactions that are not in chemical equilibrium [35, 36].

4. Summary and Conclusions

The rate limiting mechanisms of $(Ba,La)_{0.15}Sr_{0.85}FeO_{3-\delta}$ and $SrFeO_{3-\delta}$ redox reactions for solar thermochemical air separation were investigated using a combination of thermogravimetry and gas chromatography, x-ray diffractometry, and particle size characterization. Temperature- and O_2 pressure-swings were performed between 673 and 1373 K and between 100% Ar and 20% O_2/Ar, respectively, to match solar thermochemical air separation conditions. Heating/cooling rates of 10, 20 and 50 K/min were employed. Changes in deviation from stoichiometry were measured from thermogravimetry and computed as a function of temperature and O_2 partial pressures. O_2 partial pressures were measured from gas chromatography at atmospheric pressure. A compound energy formalism model was used to determine sample equilibrium conditions. Rapid thermal reduction

and oxidation chemical kinetics were observed for all experiments, suggesting heat and mass transfer as the fundamental reaction rate limiting mechanisms. Virtually no lag was observed between thermogravimetric and equilibrium changes in deviation from stoichiometry during temperature-swings for all samples during thermogravimetry, providing strong evidence that materials equilibrated quickly and were only heat transfer limited. Residual O_2 was measured during the O_2 pressure-swings as O_2 was purged for all changeovers between 20% O_2/Ar to 100% Ar. Both the thermogravimetric and equilibrium changes in deviation from stoichiometry closely followed the measured O_2 concentrations. Ba and La substitutions on the A-site did not impact the reaction rates. Sample bulk diffusion was not found to be rate limiting when comparing reaction rates for powdered and pelletized samples for masses less than 160 mg.

It is problematic to extract apparent chemical kinetics under the experimental conditions examined, since determining chemical kinetic parameters requires ultra-high heat rates to drive reactions outside of equilibrium, coupled with highly accurate O_2 concentration measurements and high-resolution spatial and temporal temperature distributions in the samples. Caution must be exercised in the determining rate limiting mechanism(s) and extracting kinetic parameters using measurements that are convoluted by the rate of O_2 purging from the system. Misidentification of kinetic parameters due to such confounding factors results in overestimated residence times for solar thermochemical and oxidation reactor heat and mass transfer models. Assuming that heat and mass transfer are the rate limiting mechanism allows for accurate performance predictions for reactors with heating rates below 50 K/min and μm-sized particles with rapid ionic diffusion of oxygen through the sublattice.

Conflicts of interest

The authors declare no conflict of interest.

Acknowledgements

References

1. T. P. Farr, N. P. Nguyen, H. E. Bush, A. Ambrosini and P. G. Loutzenhiser, *Materials*, 2020, **13**.
2. H. E. Bush, N. P. Nguyen, T. Farr, P. G. Loutzenhiser and A. Ambrosini, *Solid State Ionics*, 2021, **368**, 115692.
3. L. Wang, R. Merkle and J. Maier, *ECS Transactions*, 2019, **25**, 2497-2505.
4. B. Bulfin, L. Buttsworth, A. Lidor and A. Steinfeld, *Chemical Engineering Journal*, 2020, DOI: https://doi.org/10.1016/j.cej.2020.127734, 127734.
5. M. A. Peña and J. L. G. Fierro, *Chemical Reviews*, 2001, **101**, 1981-2018.
6. J. Dou, E. Krzystowczyk, X. Wang, T. Robbins, L. Ma, X. Liu and F. Li, *ChemSusChem*, 2020, **13**, 385-393.
7. N. Gokon, *Energy*, 2019, **v. 171**, pp. 971-980-2019 v.2171.
8. H. E. Bush, R. Datta and P. G. Loutzenhiser, *Solar Energy*, 2019, **188**, 775-786.
9. H. Falcón, J. A. Barbero, J. A. Alonso, M. J. Martínez-Lope and J. L. G. Fierro, *Chemistry of Materials*, 2002, **14**, 2325-2333.
10. R. H. Görke, E. J. Marek, F. Donat and S. A. Scott, *International Journal of Greenhouse Gas Control*, 2020, **94**, 102891.
11. E. Krzystowczyk, X. Wang, J. Dou, V. Haribal and F. Li, *Physical Chemistry Chemical Physics*, 2020, **22**, 8924-8932.
12. X. Wang, E. Krzystowczyk, J. Dou and F. Li, *Chemistry of Materials*, 2021, **33**, 2446-2456.
13. N. I. A. Malek, I. Ismail, A. M. M. Jani and N. Osman, *AIP Conference Proceedings*, 2020, **2221**, 030001.
14. S. M. Babiniec, E. N. Coker, J. E. Miller and A. Ambrosini, *Solar Energy*, 2015, **118**, 451-459.
15. A. S. Habiballah, A. M. M. Jani, A. H. Mahmud, N. Osman and S. Radiman, *Materials Chemistry and Physics*, 2016, **177**, 371-378.
16. M. T. Curnan and J. R. Kitchin, *The Journal of Physical Chemistry C*, 2014, **118**, 28776-28790.
17. T. Ishigaki, S. Yamauchi, K. Kishio, J. Mizusaki and K. Fueki, *Journal of Solid State Chemistry*, 1988, **73**, 179-187.
18. L. Wang, R. Merkle, Y. A. Mastrikov, E. A. Kotomin and J. Maier, *Journal of Materials Research*, 2012, **27**, 2000-2008.
19. A. J. Carrillo, A. H. Bork, T. Moser, E. Sediva, Z. D. Hood and J. L. M. Rupp, *Advanced Energy Materials*, 2019, **9**, 1803886.
20. B. Bulfin, J. Lapp, S. Richter, D. Gubàn, J. Vieten, S. Brendelberger, M. Roeb and C. Sattler, *Chemical Engineering Science*, 2019, **203**, 68-75.
21. B. Bulfin, J. Vieten, S. Richter, J. M. Naik, G. R. Patzke, M. Roeb, C. Sattler and A. Steinfeld, *Phys Chem Chem Phys*, 2020, **22**, 2466-2474.
22. W. Preis, E. Bucher and W. Sitte, *Solid State Ionics*, 2004, **175**, 393-397.
23. M. Ezbiri, A. Reinhart, B. Huber, K. M. Allen, A. Steinfeld, B. Bulfin and R. Michalsky, *Reaction Chemistry & Engineering*, 2020, **5**, 685-695.
24. H. E. Bush and P. G. Loutzenhiser, *Solar Energy*, 2018, **174**, 617-627.
25. A. P. Muroyama, A. J. Schrader and P. G. Loutzenhiser, *Solar Energy*, 2015, **122**, 409-418.
26. A. Le Gal and S. Abanades, *The Journal of Physical Chemistry C*, 2012, **116**, 13516-13523.
27. J. R. Scheffe, A. H. McDaniel, M. D. Allendorf and A. W. Weimer, *Energy & Environmental Science*, 2013, **6**, 963-973.

28.   A. H. McDaniel, A. Ambrosini, E. N. Coker, J. E. Miller, W. C. Chueh, R. O'Hayre and J. Tong, *Energy Procedia*, 2014, **49**, 2009-2018.

29.   M. Hillert, *Journal of Alloys and Compounds*, 2001, **320**, 161-176.

30.   M. P. Pechini, 1967, **U.S. Patent 3330697**.

31.   Y. Takashimizu and M. Iiyoshi, *Progress in Earth and Planetary Science*, 2016, **3**, 2.

32.   M. V. Bagepalli, J. D. Yarrington, A. J. Schrader, Z. M. Zhang, D. Ranjan and P. G. Loutzenhiser, *Solar Energy*, 2020, **207**, 77-90.

33.   S. A. Chizhik, S. F. Bychkov, B. V. Voloshin, M. P. Popov and A. P. Nemudry, *Chemical Engineering Journal*, 2021, **420**, 127711.

34.   I. Starkov, S. Bychkov, A. Matvienko and A. Nemudry, *Physical Chemistry Chemical Physics*, 2014, **16**, 5527-5535.

35.   H. Evan Bush, K.-P. Schlichting, R. J. Gill, S. M. Jeter and P. G. Loutzenhiser, *Journal of Solar Energy Engineering*, 2017, **139**.

36.   L. O. Schunk and A. Steinfeld, *AIChE Journal*, 2009, **55**, 1497-1504.